Supplementary Information:

Unraveling the role of Ti in the stability of positive layered ox-ide electrodes for rechargeable Na-ion batteries

Maider Zarrabeitia,[a,b,†] Elena Gonzalo,[a,†] Marta Pasqualini,[c] Matteo Ciambezi,[d] Oier Lakuntza,[a] Francesco Nobili,[c] Angela Trapananti,[d] Andrea Di Cicco,[d] Giuliana Aquilanti,[e] Nebil A. Katcho,[a] Juan M. López del Amo,[a] Javier Carrasco,[a] Miguel Ángel Muñoz-Márquez,[a]* and Teófilo Rojo[a,b]*.

[a]CIC energiGUNE, Parque Tecnológico de Álava, Albert Einstein 48, ED. CIC, 01510, Miñano, Spain

[b]Departamento de Química Inorgánica, Universidad del País Vasco UPV/EHU, P.O. Box. 664, 48080 Leioa, Spain

[c]Chemistry Division, School of Science and Technology, University of Camerino, via Madonna delle Carceri, 62032 Camerino, Italy

[d]Physics Division, School of Science and Technology, University of Camerino, via Madonna delle Carceri, 62032 Camerino, Italy

[e]Elettra – Sincrotrone Trieste, s.s. 14 km 163.5 in Area Science park 34149 Basovizza, Trieste, Italy.

[†]These authors have equally contributed to this work.

*corresponding authors: e-mail: Dr. Miguel Ángel Muñoz-Márquez: mamunoz@cicenergigune.com; Prof. Teófilo Rojo: trojo@cicenergigune.com

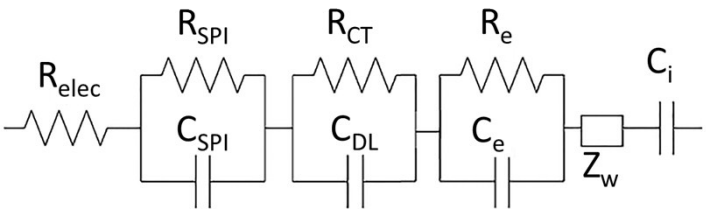

Fig. S1. The equivalent circuit used to fit the EIS data.

This model is based on:

i) At high-frequency (HF) region:

R_{elec}: electrolyte resistance when Na^+ ions cross the electrolyte from one electrode to the other.

R_{SPI}: solid permeable interphase resistance

C_{SPI}: capacitance of the electrode/electrolyte interphase

ii) At medium-frequency (MF) region:

R_{CT}: charge-transfer resistance

C_{DL}: capacitance of the double layer formed onto active particles

iii) At low-frequency (LF) region:

R_e: bulk electronic resistance

C_e: charge accumulation at the surface of the particles or at intraparticles crystallite domains

Z_w: Warburg diffusion linked to the solid-state diffusion of Na^+ ion inside the crystal

Ci: intercalation capacity due to the charge accumulation.

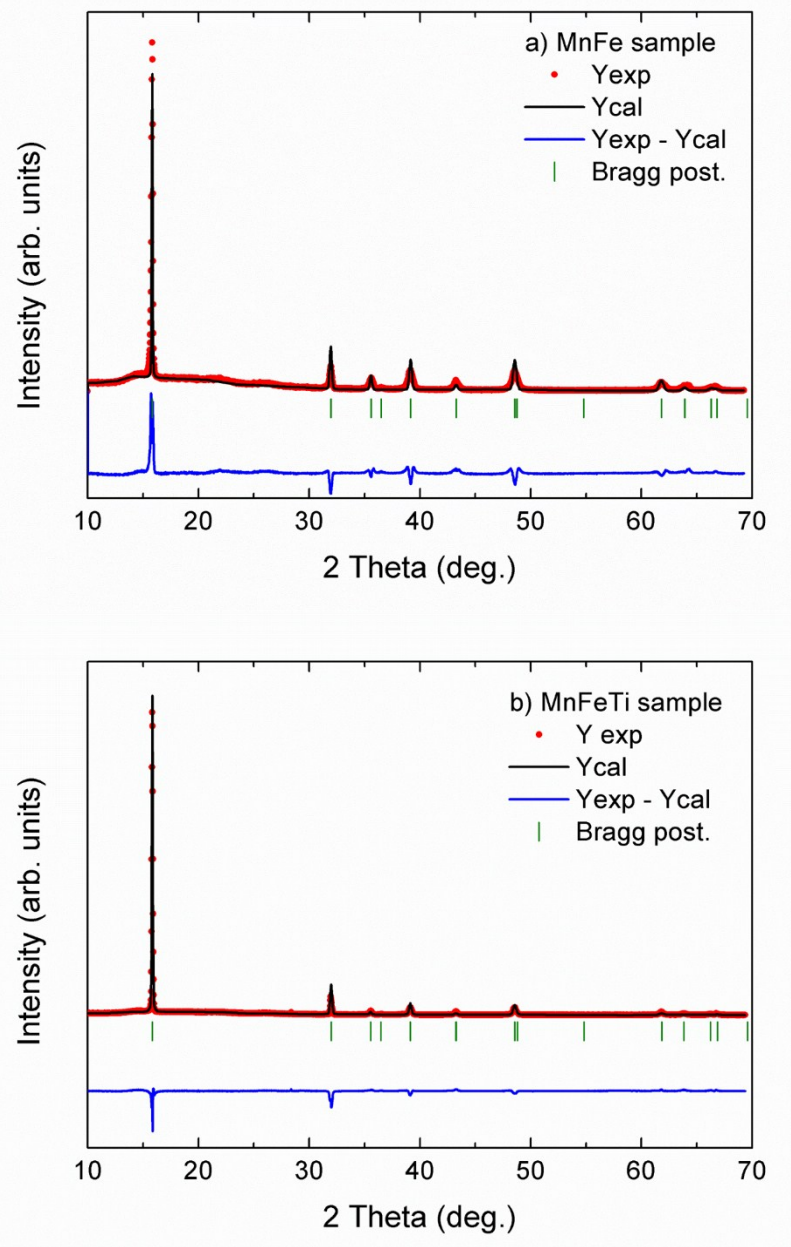

Fig. S2. PXRD patterns refined by Rietveld method with hexagonal $P6_3/mmc$ symmetry of pristine a) P2- $Na_{2/3}Mn_{0.8}Fe_{0.2}O_2$ (MnFe) and b) P2- $Na_{2/3}Mn_{0.8}Fe_{0.1}Ti_{0.1}O_2$ (MnFeTi) by FullProf software.

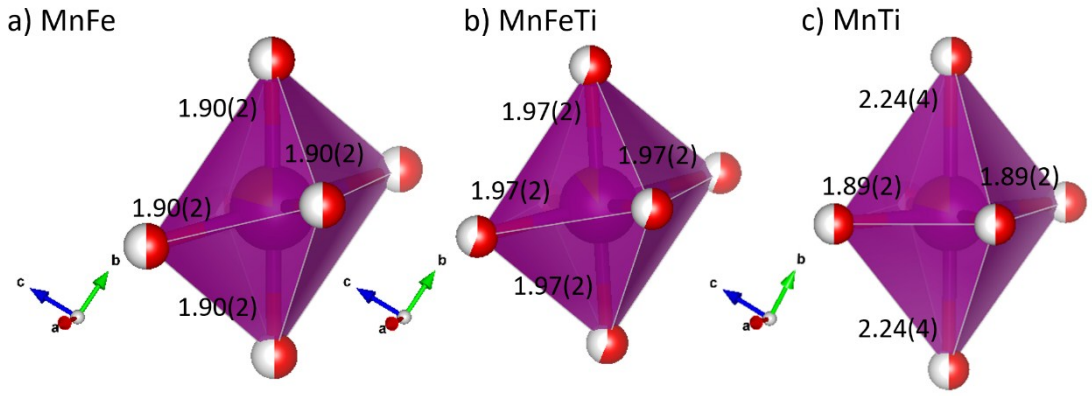

Fig. S3. [T_MO_6] octahedron (T_M = Mn, Fe and/or Ti) of a, MnFe, b, MnFeTi and c, P2-$Na_{2/3}Mn_{0.8}Ti_{0.2}O_2$ (MnTi) samples obtained by Rietveld analysis and T_M-O distances (Å).

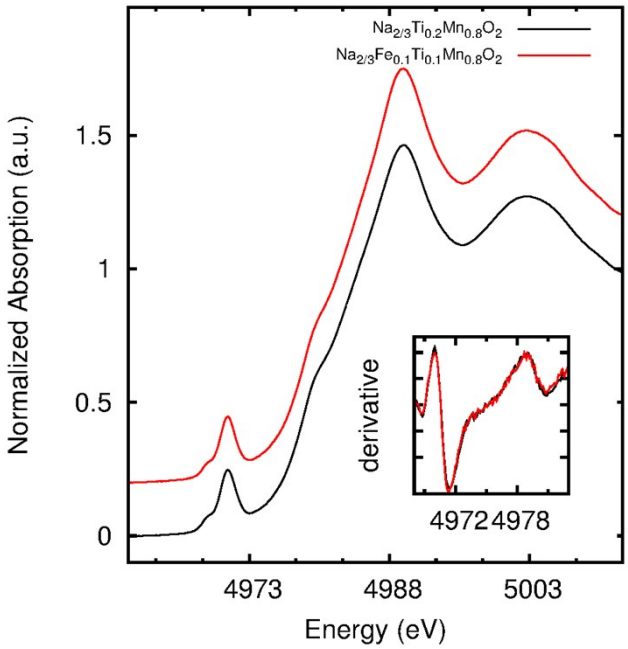

Fig. S4. Ti K-edge XANES spectra for the MnFeTi (red) and MnTi (black) and derivatives in the inset.

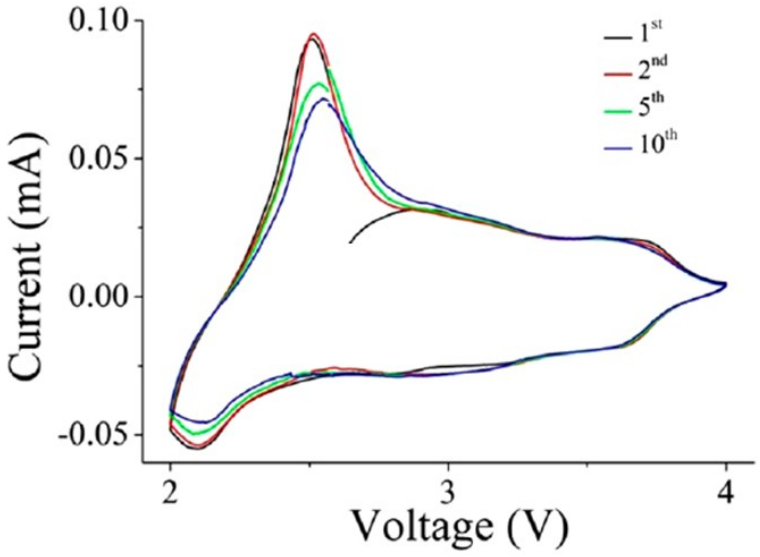

Fig. S5. Cyclic voltammetry profile of MnFeTi sample.

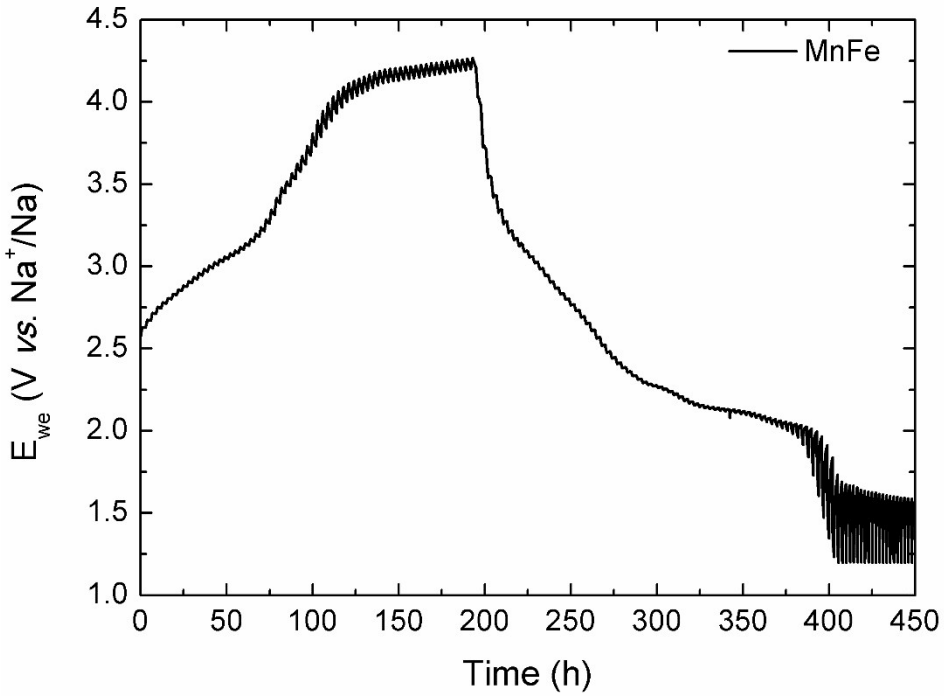

Fig. S6. GITT profile of MnFe sample.

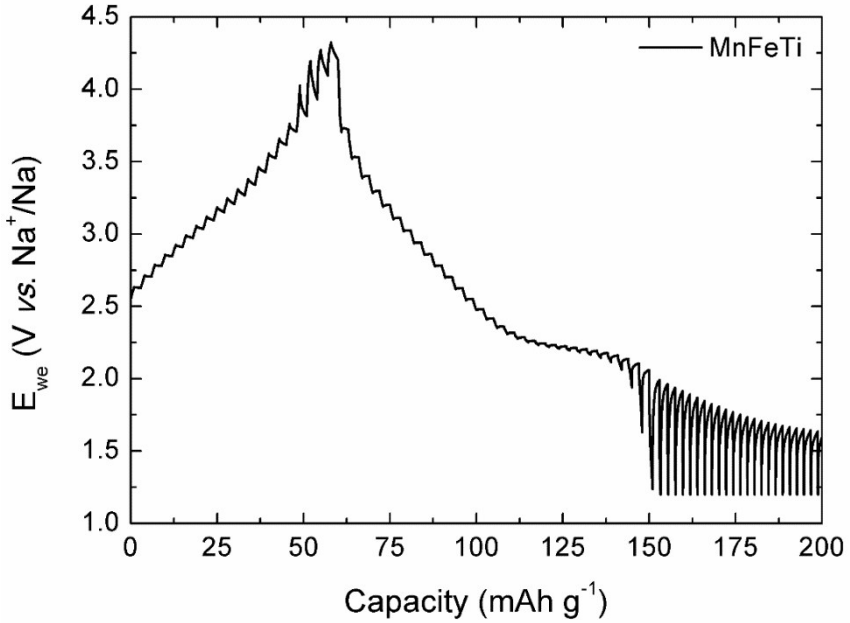

Fig. S7. GITT profile of MnFeTi sample.

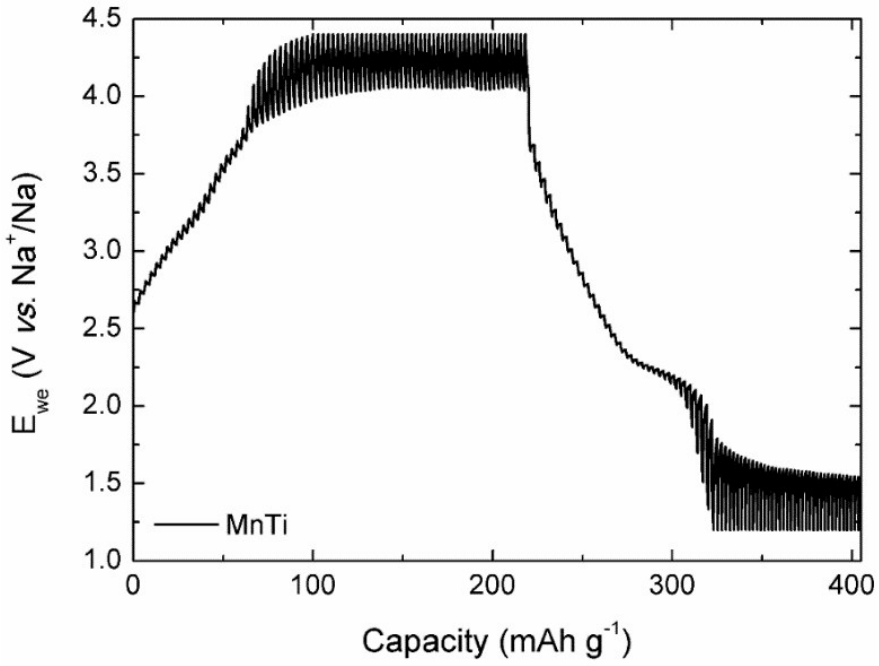

Fig. S8. GITT profile of MnTi sample.

$$D_{Na^+} = \frac{4l^2}{\pi \Delta t_p} \left(\frac{\Delta E_s}{\Delta E_t}\right)^2 \qquad \text{(Equation S1)}$$

l: characteristic diffusion length

Δt_p: galvanostatic pulse duration

ΔE_s: difference in OCV measured at the end of two sequential open-circuit relaxation step

ΔE_t: voltage change with respect to the time during the constant current pulse

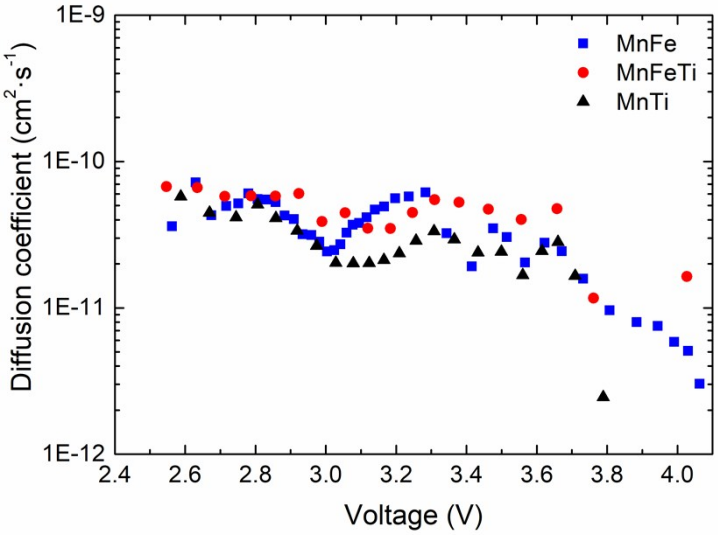

Fig. S9. D_{Na^+} vs voltage in logarithmic scale of MnFe (blue), MnFeTi (red) and MnTi (black) samples determined by GITT experiments.

The minimum of D_{Na^+} at about 3.0 V *vs* Na^+/Na is due to the reinforcement of short-range interactions between intercalating Na^+ ion and intercalating sites, thus limiting the ion mobility, around "equilibrium" potential. [1,2] Then, above 3.75 V *vs* Na^+/Na, D_{Na^+} decreases and that could be related to the complex Na^+ ion extraction process.

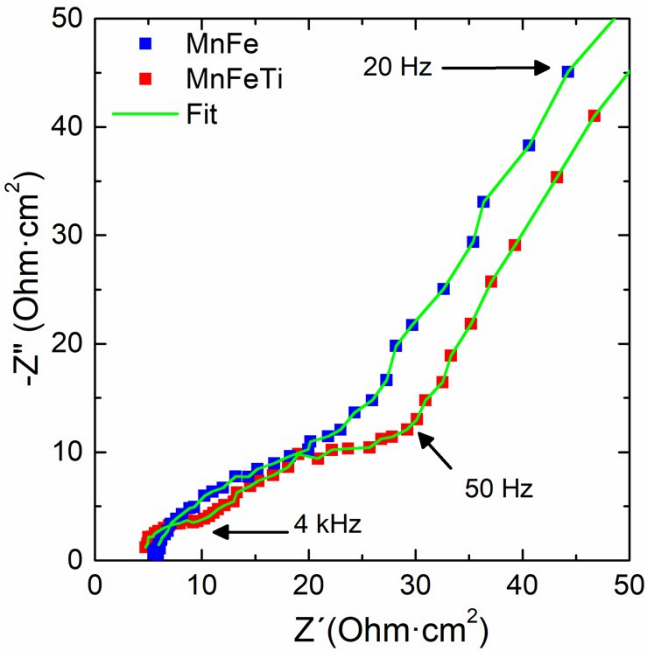

Fig. S10. Zoom of Nyquist plot of pristine electrodes of MnFe (blue squares) and MnFeTi (red squares) samples in the frequency range of 100 kHz – 20 Hz.

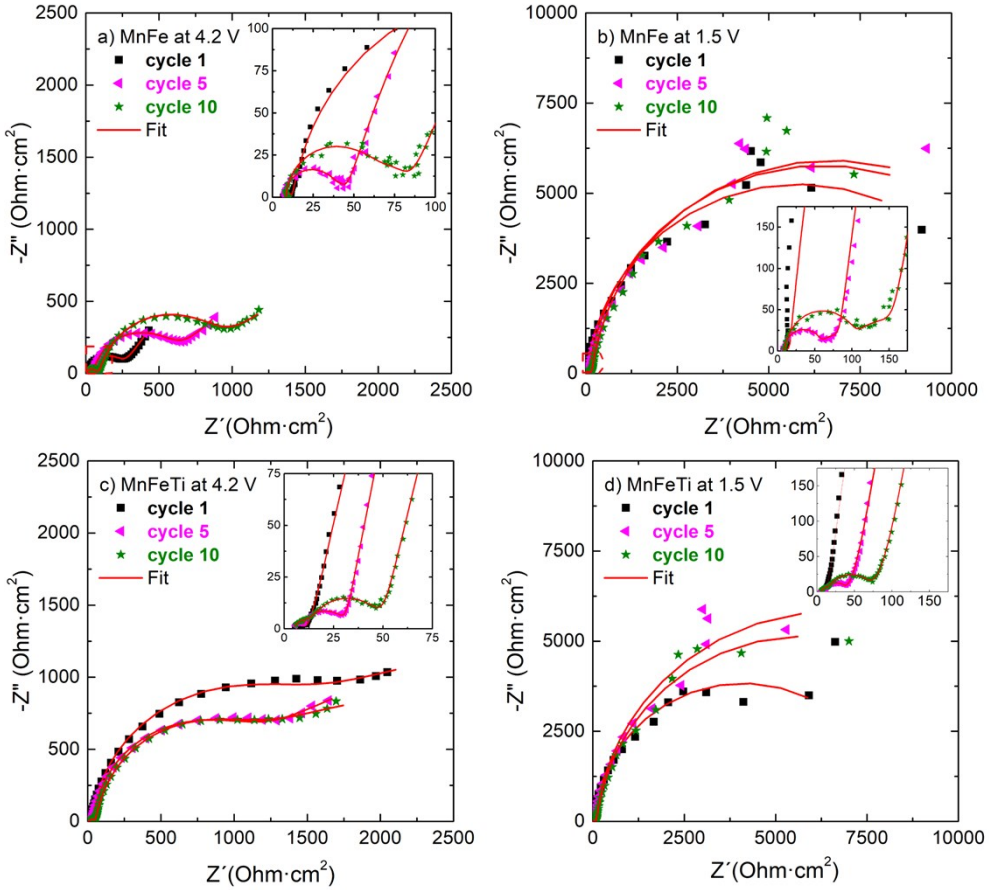

Fig. S11. Nyquist plots and corresponding fit for a), b) MnFe and c), d) MnFeTi in the frequency range of 100 kHz – 5 mHz at 4.2 V and 1.5 V vs Na^+/Na, respectively. Inset frequency range from 100 kHz to 1 Hz.

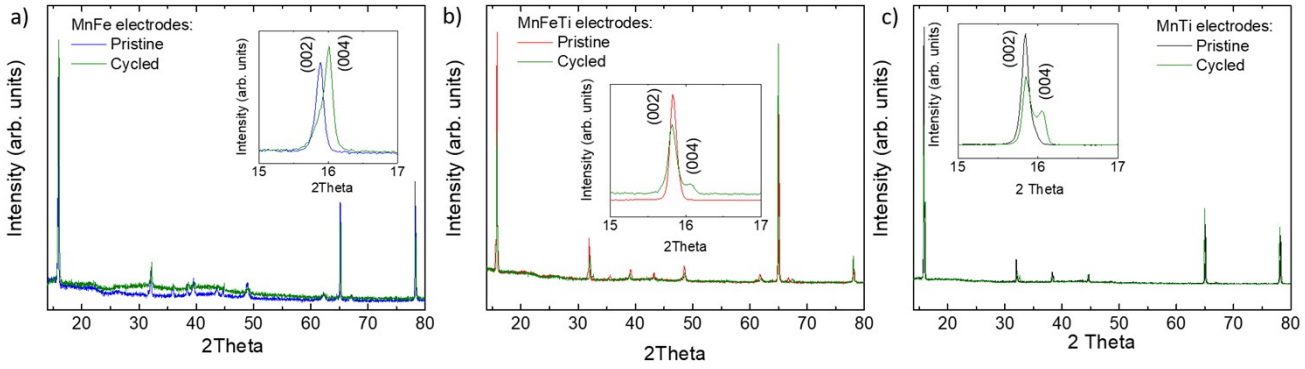

Fig. S12. PXRD patterns of a) MnFe, b) MnFeTi and c) MnTi pristine and cycled electrodes.

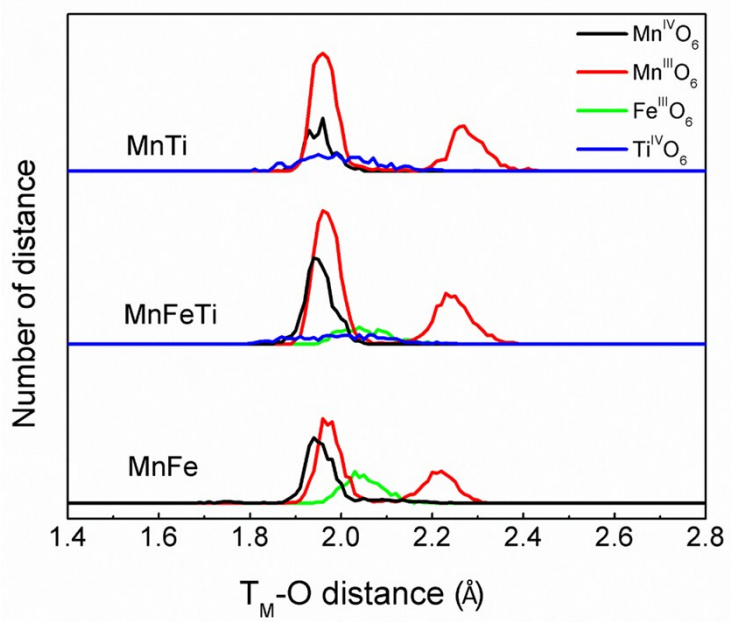

Fig. S13. T_M-O distance distributions within [T_MO_6] octahedra in MnFe, MnFeTi, and MnTi. Fe and Ti distance distributions in MnFeTi have been multiplied by two in order to facilitate the visualization.

DI expression as proposed by Warren:

$$DI = \sum_{i=1}^{6} \frac{\left| d_{MO,i} - \langle d_{MO} \rangle \right|}{6 \langle d_{MO} \rangle} \qquad \text{(Equation S2)}$$

where *i* runs over the six T_M-O bonds of the octahedron and $d_{MO,i}$ and $<d_{MO}>$ stand for the T_M-O and the averaged T_M-O distances, respectively.

Table S1. Mn oxidation state and percentage of Mn^{III} and Mn^{IV} in MnFe, MnFeTi and MnTi samples. The percentage was calculated by charge balance. On the one hand the oxidation state of each transition metal was known by XANES and Mossbauer spectroscopy and on the other hand Rietveld and ICP analysis indicate Mn:Fe, Mn:Fe:Ti and Mn:Ti ratio.

Sample	**Mn oxidation state**	**Mn^{III} (%)**	**Mn^{IV} (%)**
MnFe	+3.417	58.7	41.3
MnFeTi	+3.292	71.2	28.8
MnTi	+3.167	83.8	16.2

Table S2. The used space group, refined cell parameters and the average distance between transition metal (T_M = Mn^{IV}, Mn^{III}, Fe^{III}, Ti^{IV}) and oxygen are summarized.

Sample	Space group	Cell parameters			T_M-O distance (Å)
		a **(Å)**	***b*** **(Å)**	***c*** **(Å)**	
MnFe	$P6_3/mmc$	2.9106(2)	2.9106(2)	11.1932(7)	1.90(2)
MnFeTi	$P6_3/mmc$	2.9132(2)	2.9132(2)	11.1819(6)	1.97(2)
MnTi	$P6_3/mmc$	2.9130(9)	2.9130(9)	11.170(3)	1.97(2)
	Cmcm	2.8850(3)	5.1985(5)	11.1705(5)	2.24(4) & 1.89(2)

Table S3. Refined crystallographic parameters for pristine MnFe, MnFeTi and MnTi (taking into account both symmetries) and reliability factors.

Atom	***Wyckoff***	***x***	***y***	***z***	***SOF***
NMFO (*P*6$_3$/*mmc*)					
Mn	2*a*	0	0	0	0.8
Fe	2*a*	0	0	0	0.2
O	4*f*	0.33	0.66	0.080(3)	1.0
Na(1)	2*b*	0	0	0.25	0.33(2)
Na(2)	2d	0.33	0.66	0.75	0.34(2)
Reliability factors					
		X^2		*Rp*	*Rwp*
		4.3		5.44%	5.59%
NMFTO (*P*6$_3$/*mmc*)					
Mn	2*a*	0	0	0	0.8
Fe	2*a*	0	0	0	0.1
Ti	2*a*	0	0	0	0.1
O	4*f*	0.33	0.66	0.091(4)	1.0
Na(1)	2*b*	0	0	0.25	0.35(1)
Na(2)	2*d*	0.	0.66	0.75	0.32(1)
Reliability factors					
		X^2		*Rp*	*Rwp*
		1.79		*3.36%*	*4.32%*
NMTO (*P*6$_3$/*mmc*)					
Mn	2*a*	0	0	0	0.8
Ti	2*a*	0	0	0	0.2
O	4*f*	0.33	0.66	0.092(3)	1
Na(1)	2*b*	0	0	0.25	0.24(2)
Na(2)	2*d*	0.33	0.66	0.75	0.42(2)
Reliability factors					
		X^2		*Rp*	*Rwp*
		18.1		52.4%	45.4%
NMTO (*Cmcm*)					
Mn	4*a*	0	0	0	0.8
Ti	4*a*	0	0	0	0.2
O	8*f*	0	0.620(9)	0.906(3)	1.0

Na(1)	4*c*	0	-0.07(3)	0.25	0.31(2)
Na(2)	4*c*	0	0.62(2)	0.25	0.36(2)

Reliability factors			
	X^2	*Rp*	*Rwp*
	3.76	6.84%	6.39%

Table S4. Resultant resistance values from the fits, using the equivalent circuit detailed in Fig. S1 and shown in Fig. 4.

	MnFe	**MnFeTi**	**MnTi**
R_{elec} **(Ohm·cm²)**	5.0	4.0	1.1
R_{SPI} **(Ohm·cm²)**	2.9	4.3	64
R_{CT} **(Ohm·cm²)**	6.0	22	109
R_e **(Ohm·cm²)**	712	2,370	20,406

Table S5. Calculated DFT mean values of T_M-O distances (Å) in P2-$Na_{2/3}Mn_{0.8}Fe_{0.2-x}Ti_xO_2$. The two values in the Mn^{III} column correspond to the short (equatorial) and long (axial) distances.

x	**Mn^{IV}-O**	**Mn^{III}-O**	**Fe^{III}-O**	**Ti^{IV}-O**
0.00	1.961	1.977 / 2.213	2.049	-
0.10	1.953	1.970 / 2.246	2.051	1.999
0.20	1.953	1.964 / 2.270	-	1.997

Table S6. Average interatomic distances and corresponding variances for the three $Na_{2/3}Mn_{0.8}Fe_{0.2-x}Ti_xO_2$ samples as obtained from the EXAFS analysis. The two values correspond to the short (equatorial) and long (axial) coordination shells having coordination numbers 4 and 2 respectively.

x	**R_{Mn-O} (Å) (equatorial)**	**R_{Mn-O} (Å) (axial)**	**σ^2_{Mn-O} (10^{-3} Å^2) (equatorial)**	**σ^2_{Mn-O} (10^{-3} Å^2) (axial)**
0.00	1.940(2)	2.298(10)	8.3(8)	6.8(7)
0.10	1.944(2)	2.303(10)	7.0(7)	7.0(7)
0. 20	1.947(2)	2.297(10)	8.5(8)	7.6(8)

Supporting references

[1] F. Varsano, F. Decker, E. Masetti, F. Croce*, Electrochim. Acta* **2001**, *46*, 2069.

[2] M.D. Levi, K. Gamolsky, D. Aurbach, U. Heider, R. Oesten, *Electrochim. Acta* **2000**, *45*, 1781.